Large-Pore Mesoporous $Ho_3Fe_5O_{12}$ Thin Films with Strong Room Temperature Perpendicular Magnetic Anisotropy by Sol-Gel Processing

Christian Suchomski,[†,*] *Christian Reitz,*[†] *Damir Pajic,*[‡] *Zvonko Jaglicic,*[#] *Igor Djerdj,*[+] *and Torsten Brezesinski*[†,*]

[†]Institute of Nanotechnology, Karlsruhe Institute of Technology, Hermann-von-Helmholtz-Platz 1, 76344 Eggenstein-Leopoldshafen, Germany.

[‡]Department of Physics, Faculty of Science, University of Zagreb, Bijenička c. 32, 10000 Zagreb, Croatia.

[#]Institute of Mathematics, Physics and Mechanics & Faculty of Civil and Geodetic Engineering, University of Ljubljana, Jadranska 19, 1000 Ljubljana, Slovenia.

[+]Ruđer Bošković Institute, Bijenička 54, 10000 Zagreb, Croatia.

Abstract

We report the evaporation-induced self-assembly synthesis of large-pore mesoporous thin films of ferrimagnetic holmium iron garnet ($Ho_3Fe_5O_{12}$) from nitrate salt precursors and a polyisobutylene-*block*-poly(ethylene oxide) polymer structure-directing agent. The phase composition, atomic bonding configuration, and pore structure at the top surface and in the interior of the films were investigated by microscopy, scattering, and spectroscopy techniques, including synchrotron-based grazing incidence small-angle X-ray scattering, X-ray photoelectron spectroscopy, X-ray diffraction (including Rietveld refinement), and others. The data provide evidence that the sol–gel derived material is single phase garnet with 27 nm diameter crystallites and few defects after heating to 850 °C in air and the continuous network of pores averaging 23 nm in diameter is preserved to a large extent, despite a solid-solid conversion from metastable *h*-$HoFeO_3$ to $Ho_3Fe_5O_{12}$ during the crystallization process. Furthermore, dc magnetometry measurements show the thin films are magnetically stable with a room temperature coercivity of ~170 Oe and exhibit an out-of-plane easy axis with a significant perpendicular magnetic anisotropy. Strong preference for out-of-plane magnetic alignment in solution-processed mesostructured films is unique, making them attractive for application in spintronics and nanomagnetics.

Keywords

Rare-earth iron garnet, magnetic anisotropy, out-of-plane easy axis, sol-gel chemistry, self-assembly

Introduction

Room temperature magnetic materials are ubiquitous in modern technology and have been studied for decades. They are constantly undergoing changes to adapt to modern device requirements and, in recent years particularly, magnetic nanostructures have been in the focus of interest, with much attention paid to size and orientation effects.[1-3] Many routes to achieving nanoscale materials with different morphologies, including wires, particles, and thin films, to mention only a few, have been reported in the literature.[4-6] Among them are solution-processing routes such as solvothermal and sol–gel methods, physical deposition techniques, mechanochemical approaches, and others.[7-11] As for thin films, materials with a perpendicular magnetic anisotropy have been the subject of significant interest over the past decade due to their potential for application in nanomagnetics[12-14] (e.g., as storage/recording media) and spintronics[15-17] (e.g., as spin valves). Nevertheless, they are also highly interesting from the viewpoint of basic research.

Ferrite garnets and spinels with non-equivalent and antiferromagnetically coupled spin sublattices represent two of the most important classes of soft magnetic materials today.[18] They typically contain either transition or rare-earth cations with partially filled 3*d*- or 4*f*-shells such as MFe_2O_4 (M = Mn, Co, Ni etc.) and $RE_3Fe_5O_{12}$ (RE = Gd–Yb). Of these, the ferrimagnetic rare-earth iron garnets deserve special attention owing to their wide range of unique magneto-optical,[19, 20] magneto-caloric,[21, 22] and magneto-dielectric properties.[23, 24]

As with other metal oxides, rare-earth iron garnets have been fabricated in many different ways and forms.[25-27] However, reports on the synthesis of mesostructured films with either cubic or hexagonal pore symmetries are very scarce, although the integration of mesoporosity with

nanomagnetism might offer the possibility to broaden the scope of application of the respective materials, particularly when considering the wealth of opportunities for novel device design.

In the present work, we describe for the first time the properties of large-pore mesoporous holmium iron garnet ($Ho_3Fe_5O_{12}$, HoIG) thin films produced by facile polymer templating using an evaporation-induced self-assembly (EISA) process.[28, 29] This process goes back to Brinker and coworkers; the basics of EISA have been described in detail in many papers and are not discussed here.[30-35] Similar to our recent work on mesostructured $Y_3Fe_5O_{12}$ films,[36] the synthesis is based on the coassembly of common hydrated nitrate salts with a polymer structure-directing agent (SDA). However, unlike the yttrium compound, the HoIG thin films show no typical signs of superparamagnetism, and further exhibit a large perpendicular magnetic anisotropy. We emphasize that the property of perpendicular (out-of-plane) magnetic anisotropy is unique for solution-processed, non-textured garnet thin films. In general, preference for out-of-plane magnetic alignment in sub-micrometer-thick garnet films by overcoming the shape anisotropy is not very common and can typically only be achieved in strained epitaxial layers.[37]

Overall, we show in this paper that the EISA method can be directly applied to the synthesis of a room temperature magnetic garnet-type oxide having a strong out-of-plane easy axis. This sol–gel derived material is free of both major structural defects and impurity phases and, as we demonstrate here, can be crystallized with retention of mesoporosity. A possible mechanism for the observed magnetic anisotropy is discussed.

Experimental Section

Materials: $Fe(NO_3)_3 \times 9H_2O$ (99.99%), $Ho(NO_3)_3 \times 5H_2O$ (99.99%), absolute ethanol, tetrahydrofuran, and 2-methoxyethanol were purchased from Sigma-Aldrich and ABCR,

respectively. $H[C(CH_3)_2CH_2]_{107}C_6H_4(OCH_2CH_2)_{150}OH$ (PIB_{107}-*b*-PEO_{150})[38] was obtained from BASF SE and used as polymer SDA in this work.

Synthesis: The mesoporous HoIG thin films were prepared by mixing a solution containing 45 mg of PIB_{107}-*b*-PEO_{150} dissolved in 1.5 mL of absolute ethanol, 0.2 mL of tetrahydrofuran, and 0.5 mL of 2-methoxyethanol with both 127.4 mg of $Ho(NO_3)_3\times5H_2O$ and 194.5 mg of $Fe(NO_3)_3\times9H_2O$. The resulting reddish solution was then aged for 30 min, followed by room temperature dip-coating films on flat substrates, including quartz glass slides and Si(001) wafers, at a relative humidity (RH) of ~13% and constant pull rates in the range 5–10 mm s^{-1}. After drying the as-made films for 3 min in the dip-coater chamber, they were directly transferred to an oven at 130 °C for 2 h and then heated to 300 °C at a rate of 5 °C min^{-1}, followed by aging for 12 h. Lastly, the films were heated to 850 °C at a rate of 10 °C min^{-1}, followed by quenching to room temperature.

Methods: Transmission electron microscopy (TEM) and scanning electron microscopy (SEM) images were recorded on a CM30-ST from Philips operated at 300 kV and a MERLIN from Carl Zeiss operated at 5 kV, respectively. Tapping-mode atomic force microscopy (AFM) images were acquired on a multimode AFM from Veeco Instruments employing Olympus microcantilevers (resonance frequency = 300 kHz, force constant = 42 N m^{-1}). X-ray diffraction (XRD) measurements were carried out on a PANalytical X'Pert PRO diffractometer equipped with a Cu-Kα X-ray source and an X'Celerator RTMS detector (sample-to-detector distance = 24 cm). Grazing incidence small-angle X-ray scattering (GISAXS) patterns were collected at the light source DORIS III at DESY on beamline BW4 (λ = 0.1381 nm, beam size = 23 μm (vertical) × 30 μm (horizontal), sample-to-detector distance = 1828 mm) using a MarCCD area detector (pixel size = 79 μm, resolution = 1.97×10^{-3} nm^{-1} px^{-1}, counting time = 2×150 s). Surface

characterization by means of X-ray photoelectron spectroscopy (XPS) was performed with a VersaProbe PHI 5000 Scanning ESCA Microprobe from Physical Electronics equipped with an Al-Kα X-ray source and a hemispherical electron energy analyzer at an electron takeoff angle of 45°. The C 1*s* signal from adventitious hydrocarbon at 284.8 eV was used as energy reference to correct for charging. Raman spectra were recorded using a SENTERRA dispersive Raman microscope from Bruker Optics equipped with a YAG:Nd laser (λ = 532 nm, P = 2 mW) and an objective from Olympus (MPlan N 50x, FN = 22, NA = 0.40). N_2-physisorption data were acquired at 77 K using an Autosorb-6 automated gas adsorption station from Quantachrome Corporation. Thermogravimetric analysis (TGA) was performed on a Netzsch STA 409 PC, with the thermobalance coupled to a Balzers QMG 421 quadrupole mass spectrometer (ionization energy = 70 eV). The film thickness was determined with an Alpha Step IQ Surface Profiler from KLA Tencor. For crystal structure visualization, Crystal Impact Diamond 3.2i software was used. FullProf software was used for Rietveld refinement. Magnetic measurements were carried out on a Quantum Design MPMS XL-5 superconducting quantum interference device (SQUID) magnetometer for the temperature range 5–600 K in magnetic fields up to ±50 kOe.

Results and Discussion

The magnetic garnet thin films studied here were produced by dip-coating from a sol–gel solution using an EISA process. In this process, a polyisobutylene-*block*-poly(ethylene oxide) diblock copolymer severed as SDA.[38, 39] This amphiphilic polymer, which is also referred to as PIB_{107}-*b*-PEO_{150} in the following, is suitable for the synthesis of cubic mesoporous oxide films having both a highly crystalline wall structure and pore sizes in excess of 20 nm, as recently shown for *C*-type Yb_2O_3 and anatase/rutile TiO_2:Ta.[40, 41] One of the biggest advantages of using

PIB_{107}-*b*-PEO_{150} over other polymer SDAs is that no elaborate treatment steps or sophisticated adaptations of the EISA process are needed to make sure that the as-made composite material is well-defined at both the nanometer and micrometer length scales.

The porous properties of ~500 nm-thick PIB_{107}-*b*-PEO_{150}-templated HoIG films after crystallization at 850 °C were investigated with scanning electron microscopy (SEM), atomic force microscopy (AFM), transmission electron microscopy (TEM), and N_2-physisorption. Figure 1a shows a representative cross-sectional SEM image, which provides evidence that the network of pores persists throughout the bulk. The AFM height image in Figure 1b indicates that the films are flat with a root-mean-square (rms) roughness of equal to or less than 2 nm and the pores at the crack-free top surface are open and have an average in-plane diameter of 23 nm. This dimension is among the largest reported so far for polymer-templated mesostructured metal oxide films produced from molecular precursors without using any swelling agents. Figure 1c shows the results from TEM imaging. These are in good agreement with the surface morphology observations and reveal a cubic network of interconnected pores with walls of similar size (see also SEM, AFM, and TEM images at different magnifications in Figures S1 and S2 in the Supporting Information [SI]). The latter helps to explain why the pore-solid architecture is only affected to a limited extent during the course of crystallization. Electron diffraction and high-resolution TEM studies (see Figure S2 in the SI) demonstrate the crystallinity of the sol–gel derived material. It adopts a cubic structure with the space group $Ia\bar{3}d$ (O_h^{10}), characteristic of the garnet phase. The volume-specific Brunauer-Emmett-Teller (BET) surface area and total porosity derived from N_2-physisorption measurements are (210 ± 20) m^2 cm^{-3} and (55 ± 5)%, respectively (see type IV isotherms in Figure S3 in the SI). Assuming a density of 6.77 g cm^{-3} for HoIG, the BET value corresponds to (69 ± 5) m^2 g^{-1}. Taken together, the results described in

this section lead us to conclude that the diblock copolymer PIB_{107}-*b*-PEO_{150} produces well-defined sub-micrometer-thick mesoporous films and the pore cavities are surrounded by randomly oriented garnet crystallites after heating the material to 850 °C in air.

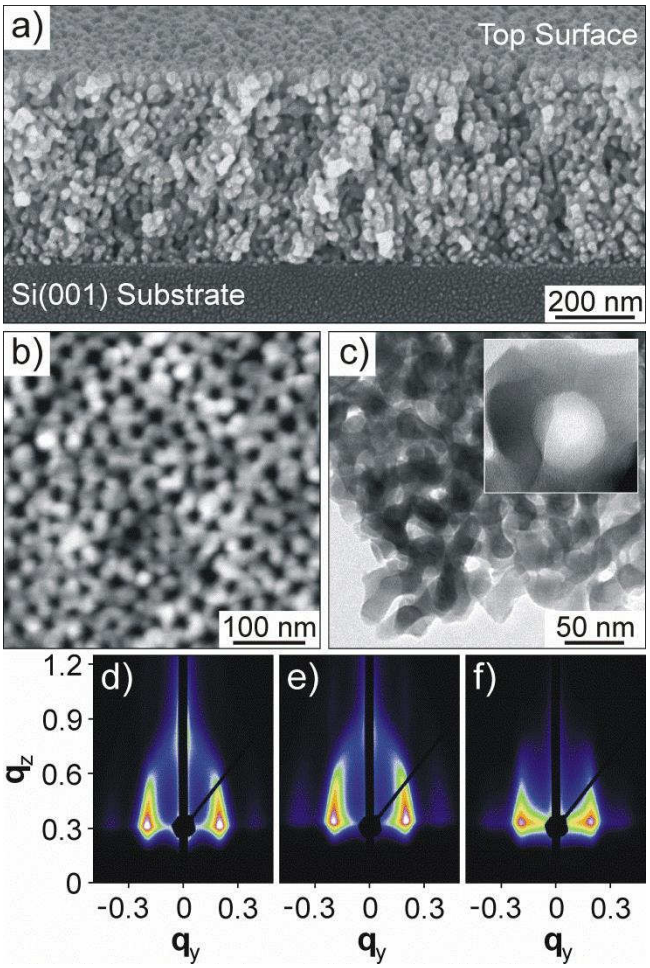

Figure 1. (a–c) Electron and force microscopy of the PIB_{107}-*b*-PEO_{150}-templated HoIG thin films heated to 850 °C: (a) cross-sectional SEM image collected with a sample tilt of 80°; (b) tapping-mode AFM height image with the contrast covering height variations in the range 0–12 nm; and (c) bright-field TEM images at different magnifications (the side length of the image in the inset is 45 nm). (d–f) GISAXS patterns at an incident angle $\beta = 0.2°$ obtained after heating a film at 300 °C for 12 h (d), and 600 °C (e) and 850 °C (f) for 1–2 s, respectively. Scattering vector $\boldsymbol{q}$ components are given in units of nm^{-1}.

To gain a better understanding of how hydrolysis and condensation reactions during heating and annealing affect the nanoscale structure, *ex situ* grazing incidence small-angle X-ray scattering (GISAXS) measurements were carried out. Figures 1d–f show GISAXS patterns obtained on a PIB_{107}-*b*-PEO_{150}-templated HoIG thin film before and after the crystallization process. It can be seen that amorphous material produces patterns with intense in-plane and out-of-plane scattering signals. These maxima can be indexed to a distorted cubic mesostructure with large repeat distances ($d_y \approx 32$ nm). As already indicated by AFM and TEM, the degree of pore ordering is not very high and is certainly less pronounced than in other polymer-templated non-silicate oxides.[31-35, 39-44] However, considering that the garnet material studied in this work is much more complex than the many binary oxides reported in the literature over the past two decades, the overall structure seems rather well-developed. The GISAXS patterns further indicate significant lattice contraction in the direction perpendicular to the substrate plane as a result of the progressive densification of the inorganic matrix and the associated release of NO_x and H_2O (see TGA-MS data in Figure S3 in the SI) upon heating; the in-plane contraction is negligible. This contraction (~75%) is completed to a large extent after annealing the films at 300 °C, thereby suggesting that the material is in a highly crosslinked state. Figure 1f shows that the scattering in the $\boldsymbol{q}_z$-direction is lost and the in-plane maxima are slightly smeared out when single phase HoIG is achieved at 850 °C, both of which can be explained by the morphological anisotropy of the films and structural changes during crystallization. Nevertheless, the GISAXS results corroborate the microscopy data and provide clear evidence that the mesostructure can be preserved up to temperatures as high as 850 °C.

The unit-cell for cubic HoIG (see Figure 2) comprises 160 atoms, equivalent to eight HoIG formula units. In this structure, which is isomorphous to naturally occurring silicate garnets such as grossularite ($Al_2Ca_3(SiO_4)_3$)[45], the Fe^{3+} ions are both tetrahedrally and octahedrally coordinated by oxygens and occupy 24*d* and 16*a* Wyckoff sites, respectively, in a ratio of 3:2.[46] The Ho^{3+} ions are located on dodecahedral 24*c* sites with eight surrounding oxygens forming a distorted cube and the O^{2-} ions sit on 96*h* sites (the oxygen coordinates *x*, *y*, and *z* differ with composition).[47] Because the Fe^{3+} ([Ar] $3d^5$) and Ho^{3+} ([Xe] $4f^{10}$) ions occupy crystallographically nonequivalent sites, they form different magnetic sublattices with antiferromagnetic spin coupling. This coupling eventually results in ferrimagnetic behavior.

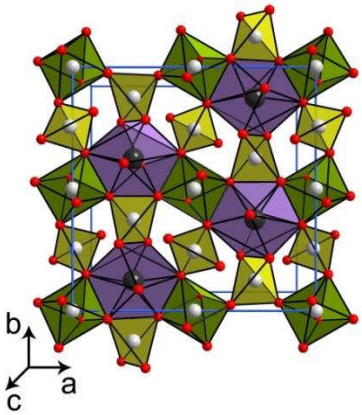

Figure 2. Unit-cell for cubic HoIG viewed along the [001] crystallographic direction. Ho^{3+} ions occupying dodecahedral 24*c* sites are shown in black, Fe^{3+} ions on both octahedral 16*a* and tetrahedral 24*d* sites in white, and O^{2-} ions on 96*h* sites in red. Only a small portion of atoms is shown for clarity.

To more fully characterize the PIB_{107}-*b*-PEO_{150}-templated HoIG thin films, particularly the phase composition, chemical state, and cation site occupancy, a series of X-ray diffraction (XRD), Raman spectroscopy, and X-ray photoelectron spectroscopy (XPS) measurements was

carried out. Representative XRD data in the range of 2θ from 25° to 33° are shown in Figure 3a. The onset of crystallization is found at $\vartheta \approx 820$ °C and polycrystalline HoIG in phase pure form is achieved by 850 °C. The broad peak centered at $2\theta = 30.8°$ is indicative of the formation of hexagonal holmium orthoferrite (h-$HoFeO_3$) with the space group $P6_3cm$ (C_{6v}^3).[48] As expected, this intermediate compound transforms into the thermodynamically stable garnet phase, rather than the orthorhombic perovskite polymorph (o-$HoFeO_3$), upon heating the films to 850 °C. We note, nevertheless, that h-$HoFeO_3$, which is isomorphous to the well-known hexagonal rare-earth manganites of the form $REMnO_3$ (e.g., multiferroic h-$HoMnO_3$), can be stabilized at the nanoscale in such mesoporous thin films (see Figure S4 in the SI). This is an exciting result, because it opens up the possibility to synthesize a new class of potential (interface-controlled) nano-multiferroics, but this goes beyond the scope of the present work. Furthermore, it is evident that the presence of larger amounts of commonly observed impurity phases such as α-Fe_2O_3, Ho_2O_3, and more complex compounds, including Ho_3FeO_6 and $Ho_4Fe_2O_9$, can be ruled out.

The high-temperature XRD pattern was also analyzed using Rietveld refinement (see Figure S5 and Table S1 in the SI for additional information). From this analysis, we find that the films heated to 850 °C in air are, in fact, single phase with lattice parameter $a = 12.354(1)$ Å ($a_{\text{equil.}} = 12.376$ Å)[46] and oxygen coordinates $x = -0.029(1)$, $y = 0.051(1)$, and $z = 0.156(1)$ and display virtually no preferred orientation. The average crystallite size is 27 nm. This dimension is in fair agreement with the wall thickness determined from AFM and TEM and provides a hypothesis for why the very same synthesis using conventional polymer SDAs failed – the vast majority produce materials with sub-10 nm-thick walls. It is important to emphasize that the mismatch that often exists between stable crystallite size and wall thickness adversely affects the synthesis of oxides possessing both a high degree of crystallinity and a well-defined porosity, thus calling

for tailor-made polymer SDAs with improved templating properties such as the diblock copolymer PIB_{107}-*b*-PEO_{150}.

Although conventional XRD is a powerful technique for analyzing crystalline materials, it is known to be less sensitive to minor amounts of impurity phases (detection limit is in the order of 1 wt.-%) than Raman spectroscopy. Therefore, Raman measurements were acquired and the results compared to experimental data for both single crystals of DyIG[49] and bulk HoIG powder. The latter was prepared from a mixture of hydrated ferric and holmium nitrate salts at 1000 °C. Figure 3b shows a set of non-polarized Raman spectra. Group theory predicts that defect-free garnets with the space group $Ia\bar{3}d$ (O_h^{10}) should have twenty five first-order Raman modes (namely, $3\times A_{1g}$, $8\times E_g$, and $14\times T_{2g}$).[50] In total, we can see fifteen bands in the frequency range 100–750 cm^{-1} (see assignment in Table S2 in the SI). Overall, our data are consistent with those for the above mentioned reference materials and confirm that the PIB_{107}-*b*-PEO_{150}-templated HoIG thin films heated to 850 °C are free of impurity phases. The lack of Raman bands is likely due to superposition of the spectra from the substrate as well as peak broadening and decreasing peak intensity as a result of finite size effects. Also, some bands apparently have nearly identical peak frequencies, as shown for single crystals of DyIG.[49] This means they can only be distinguished by polarized Raman spectroscopy. Finally, we note that we have also measured spectra of films on Si(001) substrate heated to temperatures below 850 °C. These spectra verify the formation of *h*-$HoFeO_3$ as an intermediate in the synthesis (see Figure S6 in the SI).

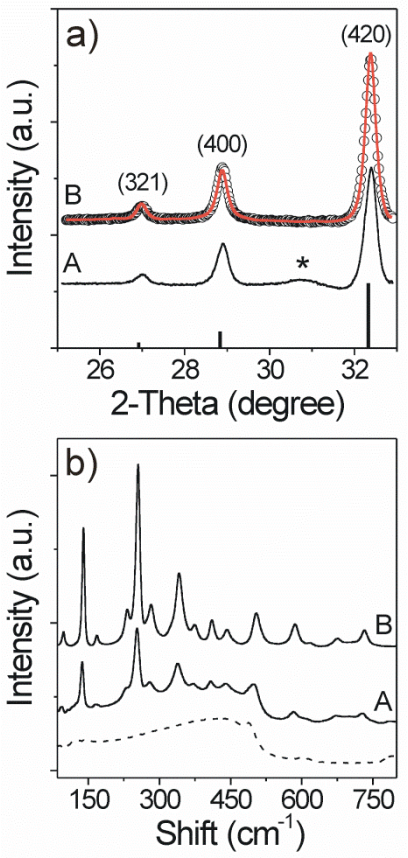

Figure 3. Crystalline structure and phase composition of the PIB_{107}-*b*-PEO_{150}-templated HoIG thin films. (a) XRD patterns recorded after heating a film to 820 °C (A) and 850 °C (B). The solid-line curve in red is a simulated pattern by Rietveld refinement and the asterisk indicates the formation of metastable *h*-$HoFeO_3$. The stick pattern shows Joint Committee on Powder Diffraction Standards (JCPDS) reference card no. 23-0282 for cubic HoIG. (b) Non-polarized Raman spectra obtained on a PIB_{107}-*b*-PEO_{150}-templated HoIG thin film on quartz glass substrate heated to 850 °C (A) and non-templated (bulk) HoIG powder heated at 1000 °C for 1 h (B). The dashed line shows a reference spectrum of pure quartz glass.

The chemical composition, atomic bonding configuration, and oxidation state of iron in the garnet structure were investigated by XPS. Figure 4 shows both a representative wide-scan

survey spectrum and detail spectra of the Fe 2*p*, Ho 4*d*, and O 1*s* levels for the PIB_{107}-*b*-PEO_{150}-templated HoIG thin films heated to 850 °C in air. In the survey spectrum in Figure 4a, only holmium, iron, carbon, and oxygen are observed. The presence of a weak C 1*s* peak is not surprising and can be explained by adventitious hydrocarbon adsorbed from the atmosphere (the crystallized films were stored under ambient conditions). The Fe 2*p* spectrum in Figure 4b was fitted using spin-orbit splitting parameters with a relative area ratio of 1:2 for the $2p_{1/2}$ and $2p_{3/2}$ component peaks, equal full width at half-maximum (FWHM) values, and with a peak separation of 13.36 eV. As is evident, it contains an asymmetric doublet due to the distribution of iron among the tetrahedral 24*d* and octahedral 16*a* sites. The appearance of distinct shakeup satellites ~8 eV higher in binding energy than the main peaks is characteristic of the oxidation state +3.[51] The peaks centered at (723.59 ± 0.02) eV and (710.23 ± 0.02) eV for the $2p_{1/2}$ and $2p_{3/2}$ levels, respectively, can be assigned to Fe^{3+} ions on tetrahedral sites and those at binding energies of (725.50 ± 0.02) eV and (712.14 ± 0.02) eV to Fe^{3+} ions on octahedral sites.[52] Interestingly, we find a peak area ratio of virtually 3:2, which suggests that antisite defects are negligible. In contrast to the Fe 2*p* data, the Ho 4*d* spectrum in Figure 4c cannot be deconvoluted readily. This is due in part to the fact that the Ho 4*d* level is partially blended with plasmon loss peaks. The O 1*s* spectrum in Figure 4d indicates two oxygen bonding states. The main peak at (529.81 ± 0.02) eV can be attributed to lattice oxygen. The minor one at (531.55 ± 0.02) eV is likely due to hydroxyl groups/adsorbed water at the top surface.[52] In summary, the XPS results demonstrate that the HoIG thin films are also well-defined at the atomic level, despite the fact that they are solution-processed.

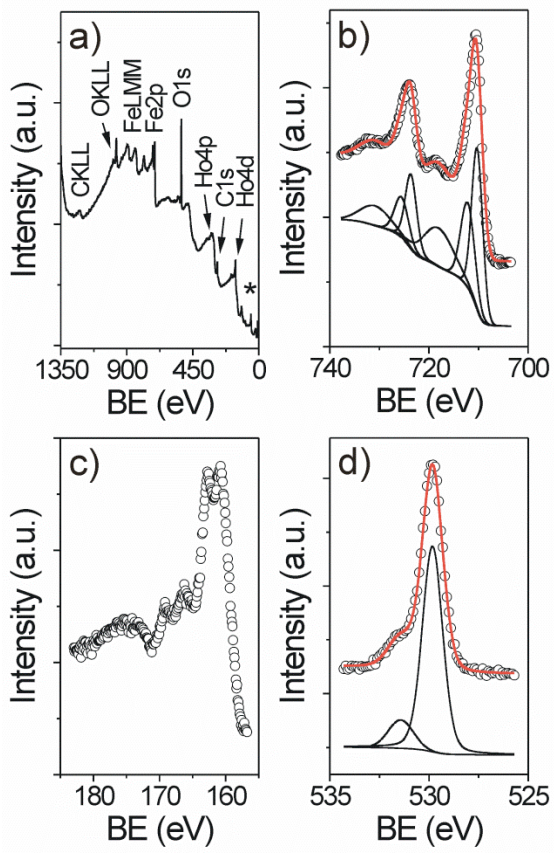

Figure 4. Chemical composition and bonding configuration of the PIB_{107}-*b*-PEO_{150}-templated HoIG thin films heated to 850 °C. (a) XPS survey spectrum. The Fe 3*s*, Fe 3*p*, Ho 5*s*, O 2*s*, and Ho 5*p* levels in the lower binding energy (BE) range are indicated by an asterisk. (b–d) XPS detail spectra of the Fe 2*p* (b), Ho 4*d* (c), and O 1*s* (d) levels. Solid-line curves in black are fits to the data and those in red are the sum of the peak fits. The Shirley method was applied to subtract backgrounds.

The temperature dependence of the in-plane and out-of-plane dc magnetization was studied by superconducting quantum interference device (SQUID) magnetometry. Figures 5a and b show zero-field-cooled (ZFC) and field-cooled (FC) curves measured in an applied field of 1 kOe. From these curves, it can be seen that (1) the ZFC data are similar for both film orientations or,

in other words, field directions, while the FC data differ from each other below ~150 K, (2) the films exhibit no typical signs of superparamagnetism, and (3) the Curie temperature, $T_C \approx 550$ K, at which the material loses its magnetic order is in the range reported in the literature ($545\ \text{K} \leq T_C \leq 567\ \text{K}$).[53-56] Overall, the ZFC data show that the sol–gel derived material starts off with a low moment and magnetization increases as the temperature is increased until a maximum is reached at (41 ± 2) K. The origin of this maximum is at present unknown, but might be associated with either some kind of spin orientation rearrangement or magnetic domain rearrangement. However, other factors might play a role as well, including film geometry and competition between sublattice exchange parameters. Thereafter, the magnetization decreases gradually until a minimum with near zero net magnetization is reached at (141 ± 4) K. This minimum results from exchange interactions between the Ho and Fe moments, with $(M_{\text{Fe(tet)}} - M_{\text{Fe(oct)}}) = -M_{\text{Ho(dod)}}$, and can be assigned to the compensation temperature, T_{comp}.[57-59]

At temperatures below T_{comp}, the FC magnetization is either positive or negative depending on the film orientation, as is evident from the data in Figures 5a and b. For the heavier rare-earth iron garnets, this magnetization-reversal transition has been shown to generally occur at high fields, in the vicinity of T_{comp}.[60-63] However, the underlying mechanism is not understood in detail. Nevertheless, it has been demonstrated that the complex behavior is closely related to the magnetic structure of the Ho sublattice – spin-ordering transition from collinear to noncollinear – and formation of a so-called magnetic umbrella structure; the Ho^{3+} ions with unquenched orbital angular momentum can be divided into different noncollinear sublattices, despite the fact that the dodecahedral 24*c* sites with local D_2 symmetry are crystallographically equivalent.[64, 65] The PIB_{107}-*b*-PEO_{150}-templated HoIG thin films show this magnetization-reversal transition at comparably small applied fields in the out-of-plane direction, thereby suggesting that the easy

axis for magnetic alignment is not likely to lie parallel to the substrate plane, as often observed for sub-micrometer-thick films due to shape anisotropy.[37] A similar observation has been made by Kalashnikova *et al*. for 10 μm-thick epitaxially grown films.[66] They found nearly square shaped out-of-plane hysteresis loops in the vicinity of T_{comp} and explained this result by growth-induced anisotropy.

Figures 5c and d show hysteresis loops for both film orientations measured at 5 K and 300 K. It can be seen that the magnetization is not completely saturated at any of the temperatures. This, however, is not unusual for nanomaterials and is often associated with surface spin canting and others size-related effects.[67-69] More importantly, the hysteresis curves confirm the magnetic easy axis as lying perpendicular to the film plane, as already indicated by the FC data. The "saturation" field is lower and the remanent magnetization and coercive fields are larger for the out-of-plane direction, which is particularly evident in the measurements at room temperature (the in-plane loop is significantly more skewed). The in-plane and out-of-plane coercivities decrease from ~4.2 kOe and ~5.8 kOe at 5 K to 40 Oe and 170 Oe at 300 K, respectively. To our knowledge, such a large perpendicular magnetic anisotropy has never been reported for polymer-templated mesoporous oxide films. Presumably, this is due to both the (uniaxial) shape anisotropy of thin films and the fact that the materials are often magnetically unstable, that is, superparamagnetic at room temperature.[70]

While we do not yet fully understand the basis for the anisotropy, we can speculate about the cause. As discussed in the section on GISAXS, the mesostructured thin films undergo significant unidirectional lattice contraction since they have only one free direction (namely, perpendicular to the film plane). This contraction is assumed to generate strain anisotropy, more specifically in-plane tensile strain (or out-of-plane compressive strain) in the lattice.[71] We note that the XRD

peak broadening also occurred because of the presence of lattice strain, which was taken into account in the Rietveld analysis. The average maximum strain ε is 0.17%. Given that HoIG has negative λ_{111} and λ_{100} magnetostriction constants,[53] such lattice distortions force the easy axis for magnetic alignment (along the [111] crystallographic direction in garnets) to lie perpendicular to the tension direction, as reported for strained epitaxial garnet thin films.[37] We presume that the preference for magnetization in the out-of-plane direction stems from a similar strain anisotropy that overcomes the strong shape anisotropy of the thin films. However, in contrast to epitaxially grown layers, this orientation effect is independent of the substrate used, because the "mechanical stress" does not result from a lattice or thermal expansion mismatch between the substrate and the film. Instead, the pore-solid architecture itself imposes the strain on the solution-processed material.

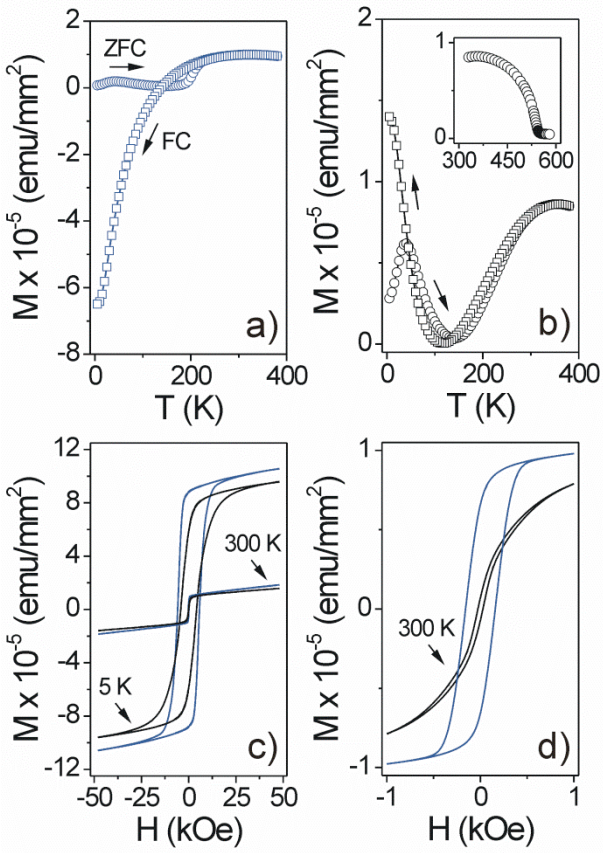

Figure 5. Out-of-plane (blue curves) and in-plane (black curves) magnetic properties of the PIB_{107}-*b*-PEO_{150}-templated HoIG thin films heated to 850 °C. (a, b) ZFC (○)/FC (□) curves measured in an applied field of 1 kOe for the temperature range 5–380 K and 300–600 K (inset). (c) Hysteresis loops at 5 K and 300 K. (d) Room temperature hysteresis loops in the field range ±1 kOe.

As mentioned above, magnetic thin films with a strong out-of-plane easy axis are of great interest for a variety of applications. Furthermore, the fact that the PIB_{107}-*b*-PEO_{150}-templated HoIG samples are stable from the magnetic point of view and have a continuous network of large mesopores renders them attractive for the development of two-phase multiferroics and other advanced nanocomposite materials (e.g., for studying exchange coupling phenomena at room temperature).

Conclusion

In summary, we have shown that high quality, single phase HoIG thin films with a large-pore mesoporous morphology and thicknesses in the sub-micrometer range can be successfully produced by facile soft-templating strategies. Remarkably, the pore network was largely preserved after crystallization, despite a partial solid-solid conversion reaction from *h*-$HoFeO_3$ to $Ho_3Fe_5O_{12}$ during the heating process in the temperature range between 820 °C and 850 °C. The nanocrystalline garnet material was found to exhibit no typical signs of superparamagnetism, which might be due in part to favorable domain coupling in the walls. In addition, significant perpendicular magnetic anisotropy was observed at room temperature. This anisotropy most likely stems from strain in the lattice caused by the unidirectional film contraction, and thus, is

assumed to be independent of the substrate. It is envisioned that the integration of nanoscale porosity with both lattice strain and confinement and interfacial effects will pave new ways of manipulating spin states in such thin films.

Author Information

Corresponding Author

*E-mail: torsten.brezesinski@kit.edu. Phone: +49 721 60828827. *E-mail: christian.suchomski@kit.edu. Phone: +49 641 9934592.

Author Contributions

All authors have given approval to the final version of the manuscript.

Funding Sources

Financial support by the German Research Foundation (T.B., grant No. BR 3499/3-1); the Unity through Knowledge Fund (www.ukf.hr) of the Croatian Ministry of Science, Education and Sports (I.D., grant No. 7/13); and the German Academic Exchange Service (T.B.) is gratefully acknowledged.

Notes

The authors declare no competing financial interest.

Associated Content

Supporting Information Available

Additional data and information from (HR)TEM, SEM, and AFM imaging, Rietveld refinement, Raman spectroscopy, N_2-physisorption, and TGA-MS. This information is available free of charge via the Internet at http://pubs.acs.org.

Acknowledgement

We thank Jan Haetge, Anneliese Heilig, Thomas Leichtweiss, and Jan Perlich for their assistance with TEM and AFM imaging, XPS, and GISAXS, respectively. Roman Zieba, Alexander Traut, and Cornelia Roeger-Goepfert from BASF SE Ludwigshafen and Bernd M. Smarsly from the Justus-Liebig-University Giessen are gratefully acknowledged for the supply of the polymer. Portions of this research were carried out at the Justus-Liebig-University Giessen and at the light source DORIS III at DESY, a member of the Helmholtz Association (HG).

References

1. Leslie-Pelecky, D. L.; Rieke, R. D. *Chem. Mater.* **1996**, *8*, 1770-1783.
2. Hehn, M.; Ounadjela, K.; Bucher, J. P.; Rousseaux, F.; Decanini, D.; Bartenlian, B.; Chappert, C. *Science* **1996**, *272*, 1782-1785.
3. Proenca, M. P.; Merazzo, K. J.; Vivas, L. G.; Leitao, D. C.; Sousa, C. T.; Ventura, J.; Araujo, J. P.; Vazquez, M. *Nanotechnology* **2013**, *24*, 475703.
4. Xia, Y. N.; Yang, P. D.; Sun, Y. G.; Wu, Y. Y.; Mayers, B.; Gates, B.; Yin, Y. D.; Kim, F.; Yan, H. Q. *Adv. Mater.* **2003**, *15*, 353-389.
5. Lu, A. H.; Salabas, E. L.; Schuth, F. *Angew. Chem. Int. Edit.* **2007**, *46*, 1222-1244.
6. Tsuchiya, M.; Sankaranarayanan, S. K. R. S.; Ramanathan, S. *Prog. Mater. Sci.* **2009**, *54*, 981-1057.
7. Titirici, M. M.; Antonietti, M.; Thomas, A. *Chem. Mater.* **2006**, *18*, 3808-3812.
8. Xu, Q.; Jarn, M.; Linden, M.; Smatt, J. H. *Thin Solid Films* **2013**, *531*, 222-227.
9. Nistor, M.; Petitmangin, A.; Hebert, C.; Seiler, W. *Appl. Surf. Sci.* **2011**, *257*, 5337-5340.
10. Schwertmann, L.; Wark, M.; Marschall, R. *RSC Adv.* **2013**, *3*, 18908-18915.
11. Coquil, T.; Richman, E. K.; Hutchinson, N. J.; Tolbert, S. H.; Pilon, L. *J. Appl. Phys.* **2009**, *106*, 034910.
12. Davies, J. E.; Giess, E. A. *J. Mater. Sci.* **1975**, *10*, 2156-2170.

13. Konishi, S. *IEEE T. Magn.* **1983**, *19*, 1838-1840.
14. Kostishyn, V. G.; Morchenko, A. T.; Chitanov, D. N. *J. Alloy. Compd.* **2014**, *586*, S317-S321.
15. Pyatakov, A. P.; Meshkov, G. A.; Zvezdin, A. K. *J. Magn. Magn. Mater.* **2012**, *324*, 3551-3554.
16. Deb, M.; Popova, E.; Fouchet, A.; Keller, N. *Phys. Rev. B* **2013**, *87*, 224408.
17. Weiler, M.; Althammer, M.; Schreier, M.; Lotze, J.; Pernpeintner, M.; Meyer, S.; Huebl, H.; Gross, R.; Kamra, A.; Xiao, J.; Chen, Y. T.; Jiao, H. J.; Bauer, G. E. W.; Goennenwein, S. T. B. *Phys. Rev. Lett.* **2013**, *111*, 176601.
18. Sugimoto, M. *J. Am. Ceram. Soc.* **1999**, *82*, 269-280.
19. Hansen, P.; Krumme, J. P. *Thin Solid Films* **1984**, *114*, 69-107.
20. Paroli, P. *Thin Solid Films* **1984**, *114*, 187-219.
21. McMichael, R. D.; Ritter, J. J.; Shull, R. D. *J. Appl. Phys.* **1993**, *73*, 6946-6948.
22. Phan, M. H.; Morales, M. B.; Chinnasamy, C. N.; Latha, B.; Harris, V. G.; Srikanth, H. *J. Phys. D Appl. Phys.* **2009**, *42*, 115007.
23. Fechine, P. B. A.; Moretzsohn, R. S. T.; Costa, R. C. S.; Derov, J.; Stewart, J. W.; Drehman, A. J.; Junqueira, C.; Sombra, A. S. B. *Microw. Opt. Techn. Let.* **2008**, *50*, 2852-2857.
24. Song, K. M.; Park, Y. A.; Lee, K. D.; Yun, B. K.; Jung, M. H.; Cho, J.; Jung, J. H.; Hur, N. *Phys. Rev. B* **2011**, *83*, 012404.
25. Popova, E.; Keller, N.; Gendron, F.; Guyot, M.; Brianso, M. C.; Dumond, Y.; Tessier, M. *J. Appl. Phys.* **2001**, *90*, 1422-1428.
26. Mergen, A.; Qureshi, A. *J. Alloy. Compd.* **2009**, *478*, 741-744.
27. Jalalian, A.; Kavrik, M. S.; Khartsev, S. I.; Grishin, A. M. *Appl. Phys. Lett.* **2011**, *99*, 102501.
28. Lu, Y. F.; Ganguli, R.; Drewien, C. A.; Anderson, M. T.; Brinker, C. J.; Gong, W. L.; Guo, Y. X.; Soyez, H.; Dunn, B.; Huang, M. H.; Zink, J. I. *Nature* **1997**, *389*, 364-368.
29. Brinker, C. J.; Lu, Y. F.; Sellinger, A.; Fan, H. Y. *Adv. Mater.* **1999**, *11*, 579-585.
30. Grosso, D.; Cagnol, F.; Soler-Illia, G.; Crepaldi, E. L.; Amenitsch, H.; Brunet-Bruneau, A.; Bourgeois, A.; Sanchez, C. *Adv. Funct. Mater.* **2004**, *14*, 309-322.
31. Sanchez, C.; Boissiere, C.; Grosso, D.; Laberty, C.; Nicole, L. *Chem. Mater.* **2008**, *20*, 682-737.
32. Innocenzi, P.; Malfatti, L. *Chem. Soc. Rev.* **2013**, *42*, 4198-4216.
33. Deng, Y. H.; Wei, J.; Sun, Z. K.; Zhao, D. Y. *Chem. Soc. Rev.* **2013**, *42*, 4054-4070.
34. Gu, D.; Schuth, F. *Chem. Soc. Rev.* **2013**, *43*, 313-344.
35. Rawolle, M.; Niedermeier, M. A.; Kaune, G.; Perlich, J.; Lellig, P.; Memesa, M.; Cheng, Y. J.; Gutmann, J. S.; Muller-Buschbaum, P. *Chem. Soc. Rev.* **2012**, *41*, 5131-5142.
36. Suchomski, C.; Reitz, C.; Sousa, C. T.; Araujo, J. P.; Brezesinski, T. *Chem. Mater.* **2013**, *25*, 2527-2537.
37. Kubota, M.; Shibuya, K.; Tokunaga, Y.; Kagawa, F.; Tsukazaki, A.; Tokura, Y.; Kawasaki, M. *J. Magn. Magn. Mater.* **2013**, *339*, 63-70.
38. von Graberg, T.; Hartmann, P.; Rein, A.; Gross, S.; Seelandt, B.; Roger, C.; Zieba, R.; Traut, A.; Wark, M.; Janek, J.; Smarsly, B. M. *Sci. Technol. Adv. Mater.* **2011**, *12*, 025005.
39. Weidmann, C.; Brezesinski, K.; Suchomski, C.; Tropp, K.; Grosser, N.; Haetge, J.; Smarsly, B. M.; Brezesinski, T. *Chem. Mater.* **2012**, *24*, 486-494.

40. Reitz, C.; Haetge, J.; Suchomski, C.; Brezesinski, T. *Chem. Mater.* **2013**, *25*, 4633-4642.
41. Reitz, C.; Reinacher, J.; Hartmann, P.; Brezesinski, T. *Catal. Today* **2013**, *225*, 55-63.
42. Smarsly, B.; Grosso, D.; Brezesinski, T.; Pinna, N.; Boissiere, C.; Antonietti, M.; Sanchez, C. *Chem. Mater.* **2004**, *16*, 2948-2952.
43. Choi, S. Y.; Mamak, M.; Coombs, N.; Chopra, N.; Ozin, G. A. *Adv. Funct. Mater.* **2004**, *14*, 335-344.
44. Ortel, E.; Reier, T.; Strasser, P.; Kraehnert, R. *Chem. Mater.* **2011**, *23*, 3201-3209.
45. Abrahams, S. C.; Geller, S. *Acta Crystallogr.* **1958**, *11*, 437-441.
46. McCarthy, G. J.; Botdorf, R.; Johnson, G. G. *J. Appl. Crystallogr.* **1972**, *5*, 377-378.
47. Euler, F.; Bruce, J. A. *Acta Crystallogr.* **1965**, *19*, 971-978.
48. Bossak, A. A.; Graboy, I. E.; Gorbenko, O. Y.; Kaul, A. R.; Kartavtseva, M. S.; Svetchnikov, V. L.; Zandbergen, H. W. *Chem. Mater.* **2004**, *16*, 1751-1755.
49. Song, J. J.; Klein, P. B.; Wadsack, R. L.; Selders, M.; Mroczkowski, S.; Chang, R. K. *J. Opt. Soc. Am.* **1973**, *63*, 1135-1140.
50. Hurrell, J. P.; Porto, S. P. S.; Chang, I. F.; Mitra, S. S.; Bauman, R. P. *Phys. Rev.* **1968**, *173*, 851-856.
51. Mullet, M.; Guillemin, Y.; Ruby, C. *J. Solid State Chem.* **2008**, *181*, 81-89.
52. Simsa, Z.; Zemek, J. *Czech. J. Phys.* **1990**, *40*, 1274-1282.
53. Sayetat, F. *J. Magn. Magn. Mater.* **1986**, *58*, 334-346.
54. Sankaranarayanan, V. K.; Gajbhiye, N. S. *J. Magn. Magn. Mater.* **1990**, *92*, 217-227.
55. Su, J.; Lu, X. M.; Zhang, C.; Zhang, J. T.; Sun, H.; Ju, C. C.; Wang, Z. J.; Min, K. L.; Huang, F. Z.; Zhu, J. S. *Physica B* **2012**, *407*, 485-488.
56. Guillot, M.; Marchand, A.; Tcheou, F.; Legall, H. *Z. Phys. B Con. Mat.* **1982**, *49*, 221-228.
57. Geller, S.; Remeika, J. P.; Sherwood, R. C.; Williams, H. J.; Espinosa, G. P. *Phys. Rev.* **1965**, *137*, 1034-1038.
58. Budkowski, A.; Szytula, A.; Rodic, D.; Duraj, R.; Mayer, J.; Sciesinski, J.; Spasojevic, V. *J. Magn. Magn. Mater.* **1989**, *78*, 226-236.
59. Guillot, M.; Tcheou, F.; Marchand, A.; Feldmann, P. *Z. Phys. B Con. Mat.* **1984**, *56*, 29-39.
60. Balanda, M.; Niziol, S. *Phys. Status Solidi B* **1979**, *91*, 291-298.
61. Levitin, R. Z.; Ponomare, B. K.; Popov, Y. F. *Sov. Phys. JETP-USSR* **1971**, *32*, 1056-1060.
62. Zvezdin, A. K.; Matveev, V. M. *Sov. Phys. JETP-USSR* **1972**, *35*, 140-145.
63. Bouguerra, A.; Fillion, G.; de Brion, S.; Khene, S.; Wolfers, P.; Hlil, E. K. *J. Phys.-Condens. Mat.* **2008**, *20*, 295231.
64. Prakash, O.; McCausland, M. A. H. *J. Phys. Solid State* **1983**, *16*, L903-L906.
65. Englich, J.; Lutgemeier, H.; Pieper, M. W.; Nekvasil, V.; Novak, P. *Solid State Commun.* **1985**, *56*, 825-828.
66. Kalashnikova, A. M.; Pavlov, V. V.; Kimel, A. V.; Kirilyuk, A.; Rasing, T.; Pisarev, R. V. *Low Temp. Phys.* **2012**, *38*, 863-869.
67. Batlle, X.; Labarta, A. *J. Phys. D Appl. Phys.* **2002**, *35*, R15-R42.
68. Jun, Y. W.; Seo, J. W.; Cheon, J. *Accounts Chem. Res.* **2008**, *41*, 179-189.
69. Pereira, C.; Pereira, A. M.; Fernandes, C.; Rocha, M.; Mendes, R.; Fernandez-Garcia, M. P.; Guedes, A.; Tavares, P. B.; Greneche, J. M.; Araujo, J. P.; Freire, C. *Chem. Mater.* **2012**, *24*, 1496-1504.

70. Eisenmenger, J.; Schuller, I. K. *Nat. Mater.* **2003**, *2*, 437-438.
71. Quickel, T. E.; Le, V. H.; Brezesinski, T.; Tolbert, S. H. *Nano Lett.* **2010**, *10*, 2982-2988.

TOC Graphic